Optical imaging of faint geosynchronous debris with the Isaac Newton Telescope

James A. Blake

Astronomy & Astrophysics Group, University of Warwick, UK

Paul Chote, Don Pollacco, Dimitri Veras

Astronomy & Astrophysics Group, University of Warwick, UK

Andrew Ash, William Feline, Nick Harwood, Grant Privett

Defence Science & Technology Laboratory, UK

ABSTRACT

In the six decades following the launch of Sputnik 1, thousands of satellites have been placed in orbit around the Earth. It has become increasingly apparent that this number is now dwarfed by a population of artificial debris originating from launch hardware, break-ups and long-term deterioration. Recent anomalies exhibited by the geostationary satellites Intelsat 29e, AMC-9 and Telkom 1 have highlighted the existence of a relatively uncharacterized population of faint debris at geosynchronous (GEO) altitudes, where there are no natural removal mechanisms. Previous attempts to catalogue these objects have employed the use of 1 m class optical telescopes, but regular monitoring is challenging, thus our knowledge remains sparse.

We conducted a blind survey of faint geosynchronous debris using eight nights of dark/grey time on the 2.54 m Isaac Newton Telescope in La Palma, Canary Islands. A total of 129 objects with on-sky angular rates consistent with GEO were detected. We probe down to $V = 21$, corresponding to objects ~ 10 cm assuming an albedo of 0.1. We compare our sampled population to those of earlier surveys. The faint end of our brightness distribution continues to grow until the sensitivity limit is reached, suggesting that the modal brightness could be even fainter. Perhaps most interestingly, a subset of faint, uncorrelated detections are rapidly tumbling such that they straddle the limiting magnitude of our observations over the course of a single exposure. These pose a rather complex issue due to the difficulty in obtaining an estimate of object size with such variation in brightness. We present a preliminary analysis based on light curves extracted from our sampled population of objects in the GEO regime.

This work is part of an ongoing collaboration between the University of Warwick and the Defence Science & Technology Laboratory to investigate the population of faint geosynchronous debris.

1. INTRODUCTION

Geosynchronous Earth orbits (GEOs) have long been sought after due to their unique orbital characteristics. A satellite placed in GEO will have a period that matches that of the Earth's rotation. To an observer on Earth, it will trace a simple analemma over the course of a sidereal day. In the special case of a geostationary orbit, a circular GEO within the equatorial plane, the satellite will remain fixed in the observer's sky. This is a property that has been exploited by communications satellites since the early 1960s.

While low Earth orbits benefit from natural decay resulting from atmospheric drag, no such removal mechanism exists for higher altitudes. In recognition of the consequently finite nature of this resource, guidelines and recommendations have been issued to address end-of-mission disposal [1]. Operators are advised to carry out a controlled manoeuvre to a so-called 'graveyard' orbit residing outside of the GEO protected region, in order to keep it clear. According to [2], compliance with these guidelines has greatly improved in recent years, with the proportion of payloads successfully clearing the protected region exceeding 80% since 2016.

Nevertheless, it must be remembered that many residents of the GEO region completed their mission long before guidelines were introduced. These uncontrolled objects are typically in drift orbits or librating around one or both of the geopotential wells that result from the non-spherical shape of the Earth [3]. A significant fraction of the drifting
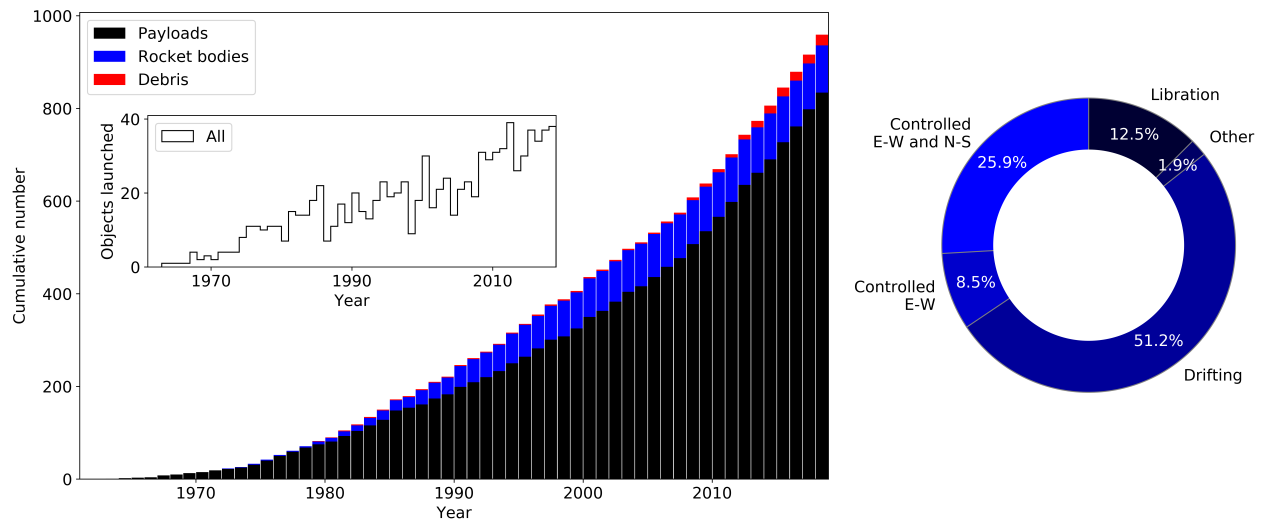
Fig. 1: The situation in GEO, as of June 2019. Left) The cumulative number of objects tracked in GEO per year, sourced from the public USSTRATCOM catalog and separated into object type. Left inset) The number of objects added to GEO each year. Right) The orbital status of tracked GEO objects, as given in [2].

objects are in elliptical and/or inclined orbits which cause them to intersect the GEO arc at 35786 km, posing a direct risk to active satellites in a like manner to those librating. With an imperfect disposal rate, orbital slots in GEO will become increasingly scarce and the risk of collision will continue to rise. This is further emphasised by the upwards trend we see in objects being added to the GEO region each year, evident in Fig. 1. It is therefore essential to closely monitor the GEO environment until a more direct form of mitigation (e.g. active removal) becomes available.

A particular concern is our lack of understanding of the faint population of debris at GEO. The publicly available USSTRATCOM catalogue provides regular two line element (TLE) updates for objects above 50-100 cm in diameter. Objects smaller than this are monitored sporadically at best, due to sensor sensitivity limitations. This is alarming, given that a recent study found relative velocities at GEO can reach up to 4 kms^{-1}, approaching energies where collisions with objects as small as 1 cm could prove mission-fatal [4]. What's more, the recent anomalies exhibited by Intelsat 29e in 2019 [5], AMC-9 and Telkom 1 in 2017 [6] have only served to highlight the existence of this uncharacterised population.

Optical techniques are typically favoured for the detection of objects at higher altitudes, as the sensitivity of optical sensors decreases with the square of the range, while that of radars decreases with the fourth power of the range. Several optical surveys have utilised telescopes with diameters of 1 m or less [7, 8, 9, 10], which typically have sensitivity limits in the range 16th–19th V Magnitude, corresponding to object sizes $\sim$ 30 cm (depending on the assumed albedo, shape and solar phase angle).

Comparatively few surveys have attempted to go fainter using larger telescopes. The Pan-STARRS or PS1 survey has dedicated some time for GEO surveillance [11], achieving a sensitivity limit of $V \sim 21$ with a 1.8 m telescope. The 6.5 m Magellan telescope at the Las Campanas Observatory in Chile has also been used to observe GEO in a limited number of spot surveys, probing to $R \sim 19$ [12]. These surveys have uncovered objects roughly 10 cm in size and found that many of them appear to be tumbling.

In order to better understand these objects, we must continue to probe the faint end of the distribution with large telescopes. To this end, we present results from a survey of faint GEO debris carried out with the Isaac Newton Telescope.

2. OBSERVATIONAL STRATEGY

We utilised eight nights of dark/grey time on the 2.54 m Isaac Newton Telescope (INT) to conduct a blind (i.e. untargeted) survey of the GEO region. The INT is based at the Roque de los Muchachos Observatory in La Palma,

Table 1: Logistical details of the observation run.

Night	Survey mode time [hrs]	Number of frames
2nd Sept 2018	8.5	608
3rd Sept 2018	7.7	552
4th Sept 2018	6.4	483
5th Sept 2018	4.5	200
6th Sept 2018	7.0	511
7th Sept 2018	6.0	455
8th Sept 2018	8.5	609
9th Sept 2018	9.4	707

Canary Islands. Table 1 summarises the data obtained in survey mode each night; in total, more than 4100 useful frames were taken over the course of 58 hours. Approximately half the night was lost on 5th Sept due to weather and technical issues. The remaining time outside of survey mode was dedicated to targeted observations of key assets and other objects of interest. These separate observations are beyond the scope of this paper.

Observations were made using the Wide Field Camera (WFC), an optical mosaic CCD camera placed at the prime focus of the INT, consisting of four thinned 2k×4k CCD chips that image over a $33'$ field of view. An issue with the readout electronics rendered one of the CCDs unusable due to excessively high readout noise. In the following photometric analysis, we discard this chip, reducing our effective field of view to $22' \times 33'$. With two-by-two binning in place, the resolution of the WFC is $0.66''\text{pixel}^{-1}$.

Numerous steps were taken to ensure our observations were optimized to suit the detection of faint GEO debris. We fixed the telescope on-sky to ensure that photons from GEO candidates would integrate over fewer pixels, thus improving the signal-to-noise ratio. In this mode, GEO objects appear as point sources or short streaks, while background stars manifest as longer streaks due to the Earth's rotation. The length of the star trails is proportional to the exposure time. An exposure time of 10 s was chosen to limit streak coverage, yet provide a sufficient integration time. We also ensured that our observations were made in close proximity to the Earth's shadow in order to minimize the phase angle between the INT, candidate objects and the Sun, thus maximising the apparent brightness of the objects. The projected angular size of the Earth's shadow cone increases as altitude decreases, so lower-altitude objects were mostly filtered out as a consequence of this strategy.

Having selected an appropriate field with these considerations in mind, we followed it throughout the night, scanning a strip of fixed declination. The INT control system is not able to acquire science images with the telescope stopped, so a custom script was used to carry out the following procedure:

1. slew the telescope to the desired field,
2. apply a differential rate offset to cancel the standard sidereal rate,
3. take a series of seven 10 s exposures,
4. recalculate the hour angle of the desired field and update the pointing,
5. repeat from step 2 until the altitude limit of $30°$ was reached.

Multiple exposures per pointing were taken to enable correlation of detected trails across frames. Simultaneous observations were obtained with a $14''$ robotic telescope, constructed from commercial-off-the-shelf (COTS) equipment. Future analysis of this additional dataset will allow for a direct comparison to be made between the detection capabilities of COTS hardware and large telescopes. We also continually scanned the GEO region using SuperWASP, a super-wide-field instrument, for the duration of the survey. This gave us coverage of the brighter targets in the vicinity of the fields surveyed by the INT. We outline our plans for a comparison study in Sec. 5.

3. DATA ANALYSIS

We developed a custom analysis pipeline to process the data from the survey, which is visually outlined in Fig. 2. The pipeline is written entirely in Python 3, and leverages a number of existing astronomical packages in order to calibrate
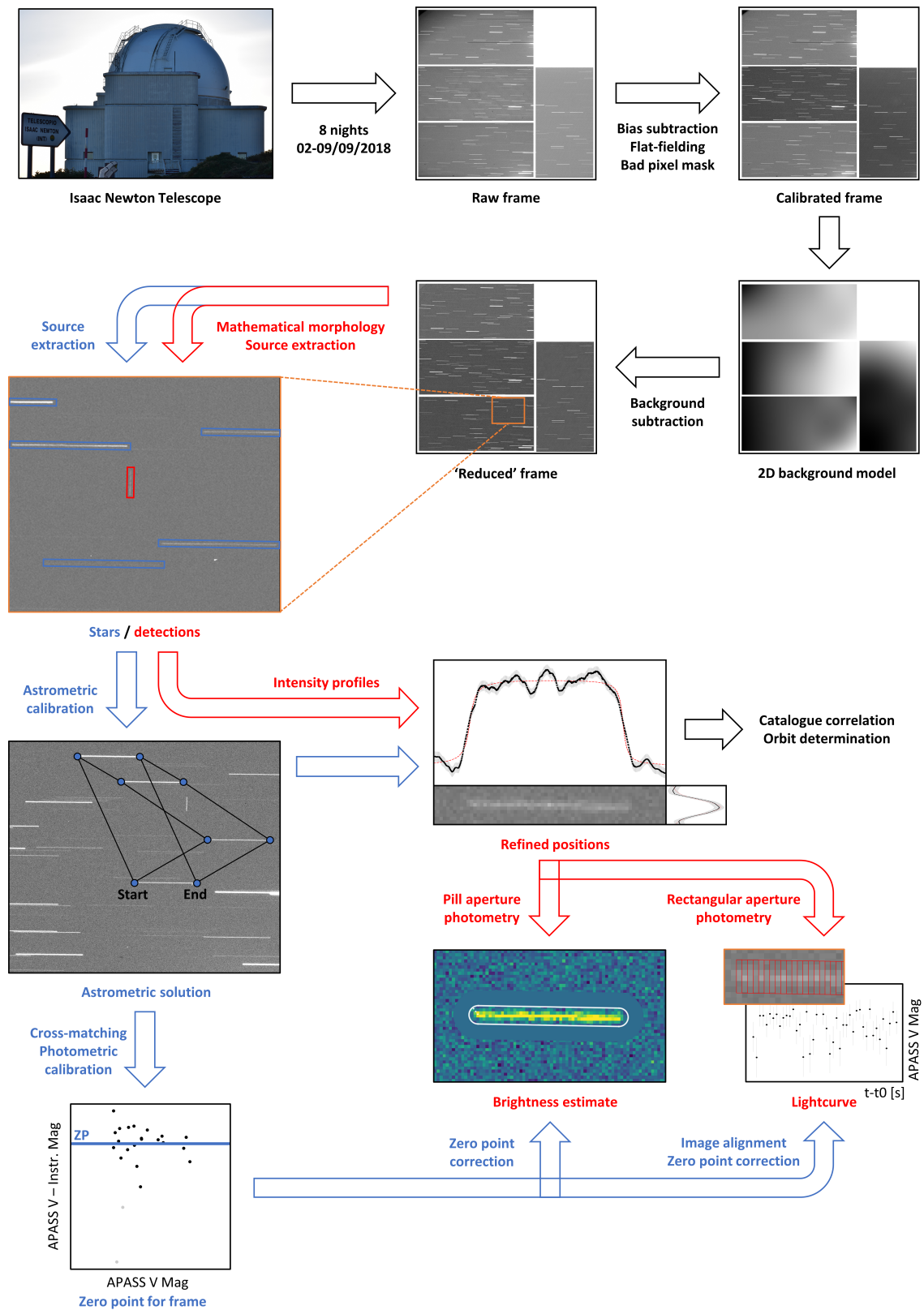
Isaac Newton Telescope

8 nights
02-09/09/2018

Raw frame

Bias subtraction
Flat-fielding
Bad pixel mask

Calibrated frame

Source extraction

**Mathematical morphology
Source extraction**

Background subtraction

'Reduced' frame

2D background model

Stars / detections

Astrometric calibration

Intensity profiles

Catalogue correlation
Orbit determination

Start   End

Astrometric solution

Refined positions

Pill aperture photometry

Rectangular aperture photometry

Cross-matching Photometric calibration

ZP

APASS V − Instr. Mag

APASS V Mag

Zero point for frame

Brightness estimate

Lightcurve

APASS V Mag

t-t0 [s]

Zero point correction

Image alignment Zero point correction

Fig. 2: The data analysis pipeline, as outlined in Sec. 3.

the raw data, detect non-astrophysical objects and extract calibrated light curves. We take inspiration from a number of previous algorithms designed to search for artificial candidates in astronomical images [13, 14, 15].

Reduction

Raw images are first processed by applying standard astronomical calibrations. Calibration frames (biases, flat fields) were taken each night and those deemed suitable were combined to form master calibrations. We use the masters to carry out bias subtraction and flat field correction. We also create a bad pixel mask consisting of 'hot' and 'cold' pixels, alongside defective pixels/columns. The masked pixels are subsequently mended with a sigma-clipped median of surrounding (good) pixels.

We then subtract the spatially varying sky background from the image. For this, we make use of SEP, a Python library based on Source Extractor, a command-line program commonly used in the field of astronomy for segmentation and extraction [16, 17]. It should be noted that the sky background map shown in Fig. 2 has an exaggerated scale; the sky contribution was very low for our observations, taken during dark/grey time.

We proceed to extract the stars by exploiting their common features, namely that they extend in the same direction and are of the same length. We use the extraction capability of SEP to carry out an initial object search with a detection threshold of three times the global background RMS. We then apply morphological cuts using the elliptical parameters determined by SEP. Trails that are oriented in the sidereal direction and of the correct length (with some allowance) are retained.

The extracted star trails are then used to perform an astrometric calibration. We feed the trail centroids and start/end points to the Linux package *Astrometry.net*, which conducts blind solving of the image frames, pattern matching subsets or 'quads' of four stars against accurate catalogues [18]. The programme has proved robust, with typical astrometric errors $(\alpha_{RA}, \alpha_{DEC}) \sim (1.5'', 0.5'')$ for solved INT frames. The package is controllable from command line and is consequently easy to wrap into our Python pipeline. After obtaining the solution, we make use of the astropy World Coordinate System (WCS) routines to convert freely between pixel and sky coordinates [19, 20].

We use the astrometric solution to obtain WCS coordinates for the extracted star trails, which are then cross-matched with the AAVSO Photometric All-Sky Survey (APASS) catalogue to enable photometric calibration of the frames. Instrumental magnitudes are derived from fluxes obtained by summing rectangular apertures placed over the trails. The instrumental magnitudes are then compared against the standard magnitudes quoted in the APASS catalogue to determine the photometric zero point for each frame.

Detection

Objects of interest can have a variety of morphologies, as evident in Fig. 3. Many GEO objects map out a simple pattern (ellipse, teardrop, figure-8) on the fixed sky over the course of a day, as opposed to remaining fixed like a geostationary satellite. The characteristics of this path are dependent on the orbital inclination and eccentricity of the object. Reflected light from such objects will be spread across a trail of pixels corresponding to the on-sky path traversed during exposure. The method of detection therefore needs to be proficient at finding non-stellar trails of varying length and orientation, in addition to the point sources expected for geostationary.

To achieve this, we construct an adaptation of the detection algorithm presented in [13]. This is based on mathematical morphology, a technique for analysing geometrical structures in binary and greyscale images. For completeness, we provide a brief overview of the mathematical formalism here. For a more detailed explanation, we refer the reader to the extensive body of literature available on the subject [21, 22, 23].

Applying some combination of morphological operations, it is possible to probe an image $f(x)$ using a structuring element B. The structuring element is a simple pixel structure that can be used to match or miss shapes within the image. A morphological transformation is achieved by scanning the image with B and assigning each pixel a value based on the structure of B and the operation in question. The simplest morphological operations are erosion ε and dilation δ, which can be expressed as

$$\varepsilon^B(f(x)) = \inf[f(x-b) : b \in B] \quad \text{and} \quad \delta^B(f(x)) = \sup[f(x+b) : b \in B]. \tag{1}$$

The erosion gives the minimum of the pixels that lie within the neighbourhood defined by B. Erosions reduce peaks and spread dark regions within the image, while dilations widen peaks and clear the dark regions.
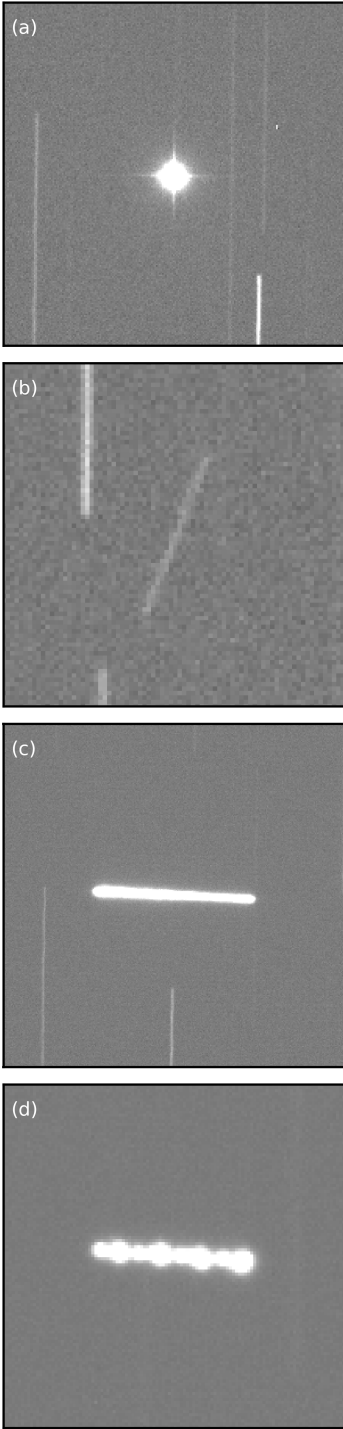
Fig. 3: Morphology examples. (a) shows a point-like geostationary satellite, while (b) is a faint GEO object with little variation in brightness. (c) and (d) show significant variability over timescales slower and faster than the exposure time, respectively.

When used sequentially, these operations give the opening O and closing C of an image. The opening operation $O^B(f(x)) = \delta^B(\varepsilon^B(f(x)))$ acts to remove small peaks, while closing $C^B(f(x)) = \varepsilon^B(\delta^B(f(x)))$ an image has the effect of removing small dark regions.

For our purposes, we follow the lead of [13], opting to make use of the Spread TopHat transformation η given by

$$\eta^B(f(x)) = f(x) - O^B(C^B(f(x))). \tag{2}$$

In this transformation, the opening of the closing is subtracted from the original image. This is performed easily using the morphology routines available in `scipy`, a Python library for scientific computing. We also carry forward the suggested structuring elements. Rectangular elements of dimensions $1 \times \frac{1}{2} l_{ST}$ pixels and $1 \times \frac{1}{6} l_{ST}$ pixels are used respectively for the opening and closing operations, where l_{ST} is the length of a star trail. This choice ensures that both elements are contained within even the fainter star trails, leading to their removal from the image. Potential GEO candidates are retained, as they do not contain the structuring element.

After carrying out this transformation, residual distractors usually remain, typically remnant edges or tips of star trails. As in [13], we find that a simple threshold cut sacrifices many of the fainter detections within our dataset. To avoid this, we first remove cosmic ray defects from the image, using the lacosmic technique implemented as part of the `ccdproc` package [24, 25]. Candidates are then extracted using SEP with a detection threshold of two times the global background RMS. We exploit our existing knowledge of star trail positions from the reduction stage of the pipeline. Detections that reside in the nearby vicinity of a known trail are checked to see if they would be fully encompassed by it and discarded if this is the case. This appears to deal well with the majority of false negatives, though some persist due to faint star trails that make it through the reductions undetected. The remaining detections are manually checked to assess their credibility. For an object to be included in the presented sample, it had to appear in at least two exposures with similar orientation and streak rate.

Refinement

The detection algorithm provides a rough estimate of object position, either via the extraction output or subsequent checks. In the case of geostationary point sources, we carry forward the centroid measured as part of the SEP extraction, as this has proved sufficiently robust. For trailed detections, however, we refine the positional estimates by fitting intensity profiles extracted along and across the trail, as shown in Fig. 2. We first use existing estimates of the start/end points to determine an approximate length and orientation for the trail. Using this information, we proceed to place circular apertures along it. The resulting intensity profile is fitted with a 'Tepui' function of the form

$$f(x) = A\left[\arctan(b_1(x - c - x_0)) - \arctan(b_2(x + c - x_0))\right], \tag{3}$$

where A is the normalised amplitude, b_1 and b_2 give the start/end slopes, c dictates the length and x_0 is a simple offset. The Tepui function has appeared frequently in the literature when tasked with fitting stellar and non-stellar streaks [26, 27, 28]. For the cross-trail profile, we opt instead for a Gaussian fit. The method used typically generates uncertainties of the order 1–3″, corresponding to ∼200–500 m at GEO. Higher uncertainties arise for blended cases. We deal with these by applying a star mask derived from the detection stage of the pipeline, which greatly improves the fit. This level of accuracy was deemed sufficient within the scope of our photometric study.
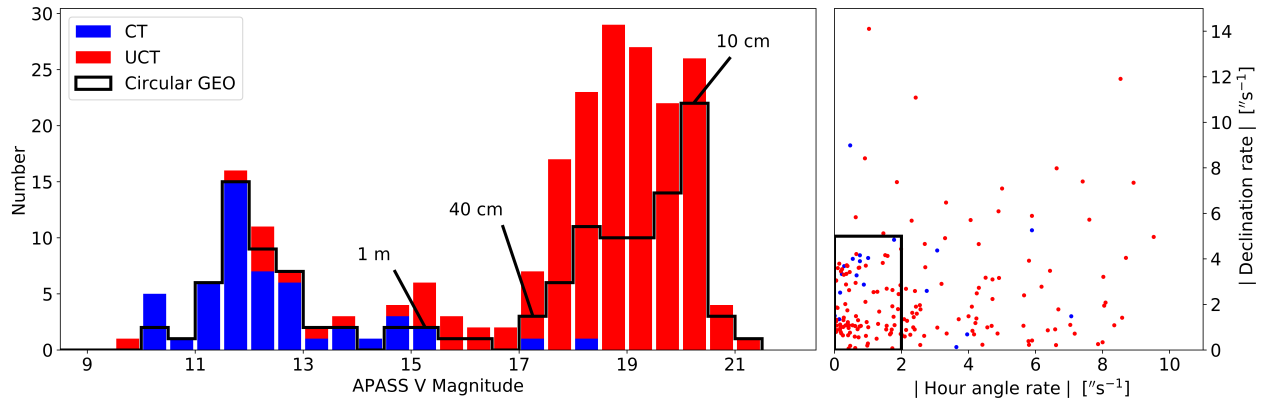
Fig. 4: Left) Histogram of brightness estimates obtained using pill aperture photometry. Objects with tracks successfully correlated (CT) with the USSTRATCOM catalogue are shown in blue, while uncorrelated tracks (UCT) are in red. The black line highlights the distribution of objects with on-sky rates expected for circular orbits in the GEO regime. Labelled size estimates assume the objects are Lambertian spheres with an albedo of 0.1. Right) On-sky angular rates for the overall dataset. Colours correspond to CT/ UCT cases as in the brightness histogram. The black box represents the rate cut used to extract the final GEO sample.

With these refined positional estimates, we achieve more accurate placement of apertures for photometric measurements. We first obtain an estimate for the total flux integrated over the course of the exposure. For this, we utilise the pill aperture available as part of the `TRIPPy` package for TRailed Image Photometry in Python [29]. The pill shape closely represents the morphology of the trailed detections and thus minimises the impact of background noise on the summation, consequently improving the achievable signal-to-noise ratio. An example placement of a pill aperture is provided in Fig. 2.

Light curves

After obtaining an estimate of total brightness, we proceed to extract light curves from the trailed detections. We place pixel-wide rectangular apertures along the trail, in such a way that no two apertures encompass the same pixel, in order to avoid the injection of correlation noise. We assume that the object is at constant speed throughout the exposure, such that it spends equal amounts of time in each aperture.

We correct for remnant background contamination (e.g. blending with star trails) by placing equivalent apertures within a reference frame. In cases where the relevant patch of sky has exited the field of view, the detection cannot be paired with a reference frame and is discarded from the light curve. We also mask sections of the light curve that are too heavily blended with background stars. In order to place the reference apertures, we first find the region of overlap between the two relevant frames. We account for any remaining offsets by feeding the overlap regions to `DONUTS`, an image alignment algorithm in Python [30]. With the reference apertures in place, we conduct an aperture-by-aperture subtraction. The corrected fluxes are converted to magnitudes using the photometrically determined zero points from the reduction stage of the analysis. Examples of the resulting light curves are provided in Sec. 4.

4. RESULTS AND DISCUSSION

In total, 226 objects were detected in survey mode over the course of the run. We apply rate cuts as in [31], retaining the objects with hour angle rates $|\text{HA rate}| < 2''\text{s}^{-1}$ and declination rates $|\text{DEC rate}| < 5''\text{s}^{-1}$. These limits are expected to include the majority of GEO candidates in circular orbits, based on findings from the NASA CCD Debris Telescope (CDT) survey [32]. Tracks with rates higher than this are likely to reside in a geosynchronous transfer orbit (GTO), an elliptical orbit with an apogee in the GEO regime. The effects of these cuts on the overall dataset can be seen in Fig. 4.

We use in-house software to carry out a correlation between the detected tracks and the USSTRATCOM catalogue. Catalogued TLEs are propagated to the time of the observation and the NORAD ID of the closest matching object is returned. A chi-squared threshold is then enforced as a correlation boundary. As evidenced in Fig. 4, we find the vast majority of uncorrelated tracks lie towards the faint end of our brightness distribution. In total, over 75% of tracks
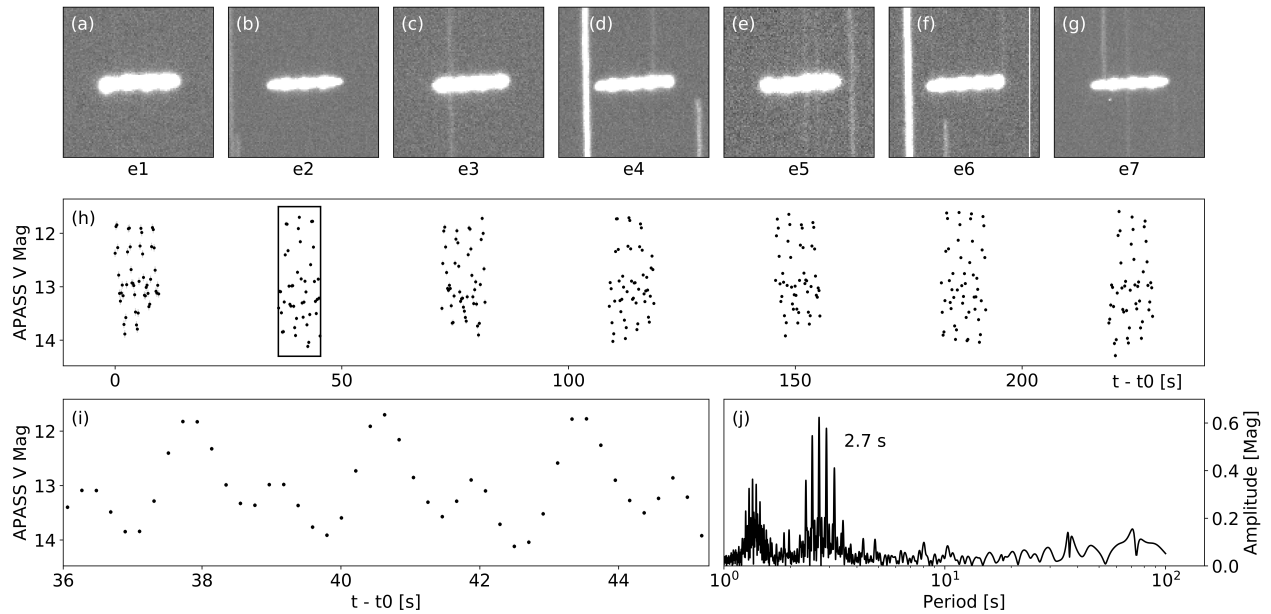
Fig. 5: Light curve analysis for a track correlated with SBS-3 (NORAD 13651), a former geostationary communications satellite. (a)–(g) show successive 10 s exposures centered on the detected trails. The overall light curve extracted using the method outlined in Sec. 3 is given in (h), while (i) zooms in to the highlighted region. The Fourier amplitude spectrum in (j) uncovers a signal with period 2.7 s. Splitting of the peaks arises due to the large readout-induced gaps between our exposures.

failed to correlate. A lack of correlation for bright objects can likely be attributed to limitations associated with the available TLEs, a topic outside the scope of this paper.

In total, 129 objects survive the imposed rate cuts, making up our final GEO sample. This gives us a detection rate of $\sim 11 \, \text{hour}^{-1} \text{deg}^{-2}$ for objects likely to reside in GEO. Similar rates have been observed for the Magellan studies [31]. The Magellan 6.5 m is located in Chile, proximate in longitude to the geopotential well at $105°$ W. A higher density of debris would be expected owing to the libration of trapped objects. Indeed, risk analyses for GEO have predicted that collisions are up to seven times more likely to occur in these regions [3]. From our vantage point on La Palma ($\sim 18°$ W), we are situated almost directly inbetween the two wells. Thus, we would intuitively expect to have a lower detection rate. However, it must be remembered that both the Magellan and INT surveys are preliminary investigations and consequently suffer from small number statistics. It is therefore difficult to draw a conclusion from these detection rates at such an early stage. Plans to extend our search are outlined in Sec. 5.

Our results are consistent with earlier studies that found a bimodal brightness distribution. The bright, correlated end peaks around 12th V Magnitude, in agreement with findings from the ESA GEO surveys [33]. The ESA 1 m is based in Tenerife and thus samples the same region of the geostationary belt as the INT. The faint end of our overall distribution seems to plateau around $V = 19$, before dropping off sharply at our sensitivity limit of $V \approx 21$. When we instead consider the GEO sample, the faint end continues to rise until the sensitivity limit, implying that the modal brightness of the population may lie even fainter.

If we make the typical assumptions that our objects are Lambertian spheres with an albedo of 0.1 [34], we probe down to diameters $d < 10$ cm. However, these assumptions are uncertain, with no *a priori* knowledge of the object's nature available in most cases. Estimating a size becomes particularly difficult when a track varies in brightness over the course of an exposure.

In Fig. 5, we show the light curve extracted for a track correlated with SBS-3 (NORAD 13651), a former geostationary communications satellite that now resides in a graveyard orbit. The satellite is based on the Hughes HS-376 model, consisting of a cylindrical bus with extended antennas. The satellite's light curve is exhibiting a strong periodic signal, indicating some form of tumbling motion. The Fourier amplitude spectrum detects a period of 2.7 s for the repeated
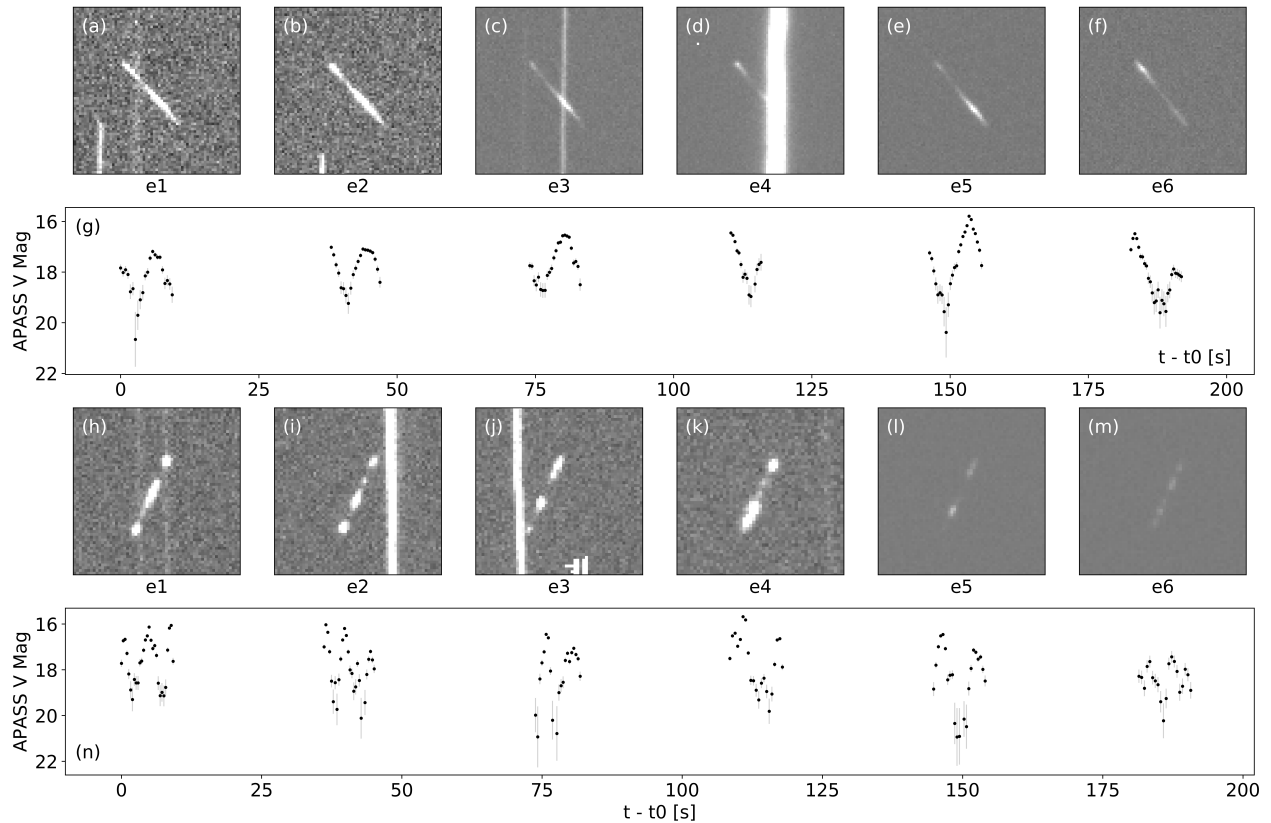
Fig. 6: Light curves for two uncorrelated detections. (a)–(f) show successive 10 s exposures for the first object, while (g) gives the extracted light curve. The 10 s exposures for the second object in (h)–(m) are flipped in the horizontal direction to align with the corresponding light curve in (n).

pattern. This period is potentially a higher-frequency harmonic of the the true tumbling period, resulting from the geometrical symmetry of the satellite bus, as reflective components like solar panels repeatedly tumble in and out of view. Previous studies have attempted to separate the dynamical and geometrical components of GEO light curves in an effort to characterise the satellite observed, though it is a notoriously difficult endeavour, complicated by the evolution of the satellite while in orbit [35, 36, 37, 38, 39]. Comparatively little has been done for smaller debris, owing to the difficulty in obtaining a usable sample. Observations of these faint, uncontrolled objects will play a key role in understanding the perturbative forces at GEO and thus the long-term evolution of the debris environment.

We find signs of tumbling in many light curves of faint, uncorrelated objects. Most interestingly, a subset of fainter detections straddle the limiting magnitude of our observations, such that the brightness profile repeatedly drops into the background noise. In addition to the lack of *a priori* knowledge of the object's nature for these cases, there is also no clear estimate of brightness from which to infer a size.

Examples of these faint, tumbling objects are provided in Fig. 6. The first track shows a significant variation in brightness with a period that may be similar to the exposure time. The object's brightness ranges from 16th to 20th *V* Magnitude, implying that highly reflective material is repeatedly tumbling in and out of view. A similar range in brightness is observed in the second light curve, though this shows more complex structure to the signal. This likely results from either a higher number of reflective surfaces or more complex rotational dynamics.

Further examples of extracted light curves are provided in Fig. 7. Panels (a) to (c) show analysis for an object correlated with an SL-12 rocket body (NORAD 16797). The amplitude spectrum shows a peak at 3.4 s, a higher frequency than expected from the sample of rocket bodies in [40]. Once again, this could simply be a high frequency harmonic of the true tumble period. The second light curve in Fig. 7 is for a faint, uncorrelated object that appears to be tumbling with a period longer than the exposure time. Observing in blind survey mode clearly leads to an undersampling of this
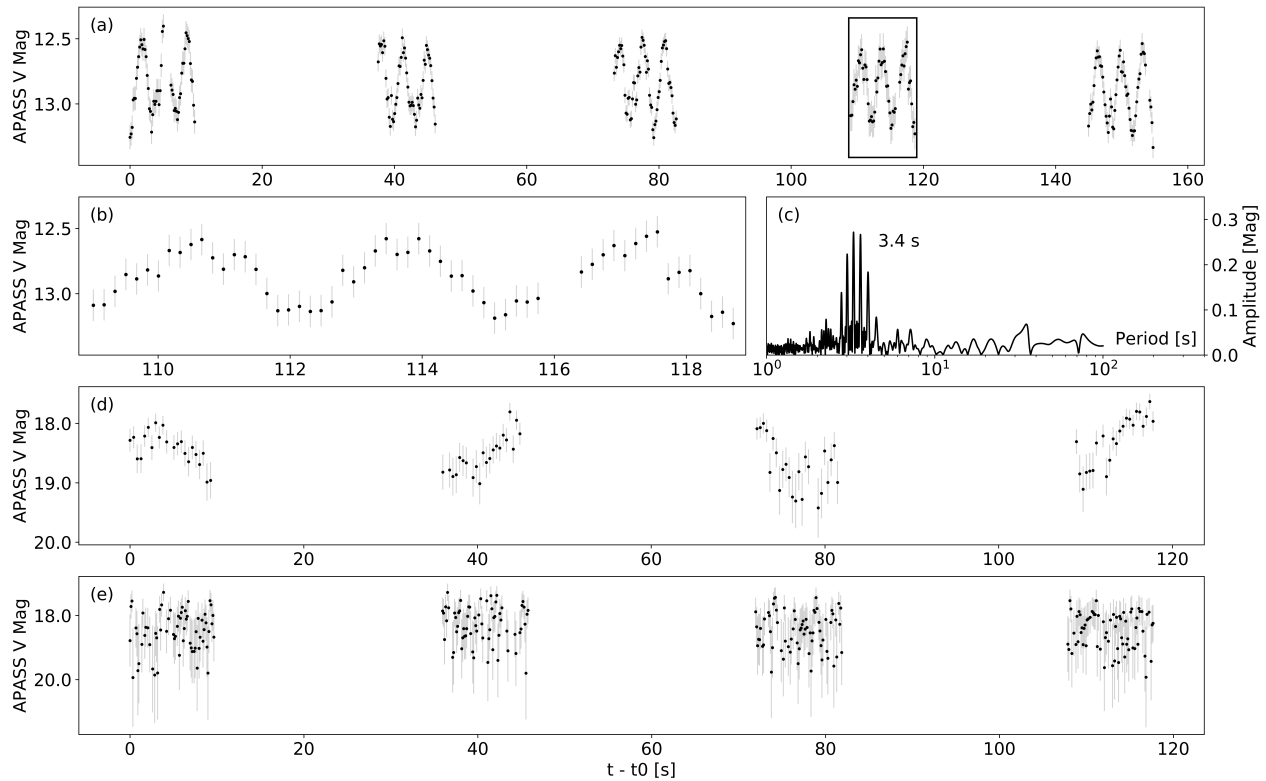
Fig. 7: Light curves for three detected tracks. The light curve in (a) corresponds to an object correlated with an SL-12 rocket body. Panel (b) zooms in to the highlighted region. We obtain the Fourier amplitude spectrum given in (c), finding a prominent peak at 3.4 s. (d) and (e) show the light curves of two uncorrelated tracks, the first tumbling with a period longer than the exposure time, the second with little variation during the observation window.

type of brightness profile. The object would need to be observed for a longer period of time to have any confidence in extracting an average brightness. The third light curve instead shows very little variation in brightness over the course of the observations. The corresponding object likely has a uniform reflectivity across its surface, or may have been oriented in such a way that reflective regions remained hidden from view during our exposures.

It is clear that tumbling is a prevalent issue when investigating the faint population of GEO debris. With order of magnitude changes in brightness, the usual assumptions regarding object shape and albedo completely break down, especially when the brightness level drops below the limiting magnitude of the observing instrument. Thus, it becomes difficult to interpret the faint end of the brightness distribution.

5. FUTURE PROJECTS

This paper presents results from an ongoing study of the faint population of GEO debris, focusing on preliminary photometric analysis. With the full sample of light curves extracted, we wish to investigate the distribution of brightness variability across orbital parameter space. To this end, it will be necessary to determine orbits from our positional estimates. Application of the standard Gauss angles-only method [41] to our data has failed to generate realistic results, prompting us to consider short-arc orbit determination methods [42] in order to better identify admissable regions. The orbital analysis will form the basis of a follow-up study that builds on the photometric findings presented thus far.

As mentioned in Sec. 2, we carried out simultaneous observations with a $14''$ robotic telescope, slaved to the INT during survey mode. Temporarily installed in La Palma, this Rowe-Ackermann Schmidt Astrograph (RASA) has a $3.6° \times 2.7°$ field of view and achieves a resolution of $1.6''\text{pixel}^{-1}$. The RASA observations will provide an excellent opportunity to test the capability of COTS equipment when tasked with surveying debris at GEO. Analysis of the paired observations will be presented in a separate study.

Lastly, we hope to extend our search for faint GEO debris by gaining more time on large telescopes. We welcome any collaborative proposals with this goal in mind.

6. SUMMARY

We present photometric analysis from a blind survey of faint geosynchronous debris carried out with the 2.54 m Isaac Newton Telescope in La Palma, Canary Islands. Using a custom Python analysis pipeline, we detect 226 objects, 129 with on-sky angular rates consistent with the GEO regime. We find a bimodal brightness distribution, the faint end of which continues to increase until the sensitivity limit of the instrument is reached. By extracting light curves from the trailed detections, we explore brightness variability exhibited by a number of our objects. Intriguingly, we uncover a subset of faint, uncorrelated objects that are tumbling in and out of the limiting magnitude of our observations. In order to fully understand this subset of the sampled population, we must continue to probe the faint end of the distribution with large telescopes. This will be critical to understanding the risk posed to active satellites in GEO and hence the long-term sustainability of the GEO environment.

7. REFERENCES

[1] IADC. In *Proceedings of 15th Inter-Agency Space Debris Coordination Committee Meeting*, 1997.

[2] ESA's Annual Space Environment Report. GEN-DB-LOG-00271-OPS-SD(3.1), 2019.

[3] D. S. McKnight and F. R. Di Pentino. New insights on the orbital debris collision hazard at GEO. *Acta Astronautica*, 85:73–82, 2013.

[4] D. L. Oltrogge et al. A comprehensive assessment of collision likelihood in Geosynchronous Earth Orbit. *Acta Astronautica*, 147:316–345, 2018.

[5] C. Henry. Intelsat-29e declared a total loss. *SpaceNews*, 2019.

[6] P. M. Cunio et al. Photometric and Other Analyses of Energetic Events Related to 2017 GEO RSO Anomalies. In *Proceedings of the Advanced Maui Optical and Space Surveillance Technologies Conference*, 2017.

[7] T. Schildknecht. Optical surveys for space debris. *The Astronomy and Astrophysics Review*, 14(1):41–111, 2007.

[8] F. Alby et al. Status of CNES optical observations of space debris in geostationary orbit. *Advances in Space Research*, 34(5):1143–1149, 2004.

[9] E. Barker et al. The GEO environment as determined by the CDT between 1998 and 2002. In *4th European Conference on Space Debris*, volume 587, page 135, 2005.

[10] P. Seitzer et al. Modest observations of space debris at geosynchronous orbit. *Advances in Space Research*, 34(5):1139–1142, 2004.

[11] M. Bolden, P. Sydney, and P. Kervin. Pan-STARRS status and GEO Observations Results. Technical report, Air Force Research Lab Kihei Maui HI Detachment 15, 2011.

[12] P. Seitzer et al. The Population of Optically Faint GEO Debris. In *Proceedings of the Advanced Maui Optical and Space Surveillance Technologies Conference*, 2016.

[13] M. Laas-Bourez et al. A new algorithm for optical observations of space debris with the TAROT telescopes. *Advances in Space Research*, 44(11):1270–1278, 2009.

[14] M. Levesque. Automatic reacquisition of satellite positions by detecting their expected streaks in astronomical images. In *Proceedings of the Advanced Maui Optical and Space Surveillance Technologies Conference*, 2009.

[15] G. Privett et al. An Autonomous Data Reduction Pipeline for Wide Angle EO Systems. In *Proceedings of the Advanced Maui Optical and Space Surveillance Technologies Conference*, 2017.

[16] K. Barbary. SEP: Source Extractor as a library. *The Journal of Open Source Software*, 1(6):59, 2016.

[17] E. Bertin and S. Arnouts. SExtractor: Software for source extraction. *Astronomy and Astrophysics Supplement Series*, 117(2):393–404, 1996.

[18] D. Lang et al. Astrometry.net: Blind astrometric calibration of arbitrary astronomical images. *The Astronomical Journal*, 139(5):1782, 2010.

[19] T. P. Robitaille et al. Astropy: A community Python package for astronomy. *Astronomy & Astrophysics*, 558:A33, 2013.

[20] A. M. Price-Whelan et al. The astropy project: building an open-science project and status of the v2.0 core package. *The Astronomical Journal*, 156(3):123, 2018.

[21] E. J. Breen, R. Jones, and H. Talbot. Mathematical morphology: A useful set of tools for image analysis. *Statistics and Computing*, 10(2):105–120, 2000.

[22] G. Matheron and J. Serra. The birth of mathematical morphology. In *Proceedings of the 6th International Symposium of Mathematical Morphology*, pages 1–16. Sydney, Australia, 2002.

[23] J. Serra and P. Soille. *Mathematical morphology and its applications to image processing*, volume 2. Springer Science & Business Media, 2012.

[24] P. G. Van Dokkum et al. Cosmic-ray rejection by Laplacian edge detection. *Publications of the Astronomical Society of the Pacific*, 113(789):1420, 2001.

[25] M. W. Craig et al. ccdproc: CCD data reduction software. *Astrophysics Source Code Library*, 2015.

[26] F. J. Montojo, T. L. Moratalla, and C. Abad. Astrometric positioning and orbit determination of geostationary satellites. *Advances in Space Research*, 47(6):1043–1053, 2011.

[27] S-Y Park et al. Development of a data reduction algorithm for optical wide field patrol (OWL) II: improving measurement of lengths of detected streaks. *Journal of Astronomy and Space Sciences*, 33(3):221–227, 2016.

[28] E. Lacruz et al. High Astrometric Precision in the Calculation of the Coordinates of Orbiters in the GEO Ring. *Revista Mexicana de Astronomía y Astrofísica*, 54:209–216, 2018.

[29] W. Fraser et al. TRIPPy: trailed image photometry in python. *The Astronomical Journal*, 151(6):158, 2016.

[30] J. McCormac et al. DONUTS: A science frame autoguiding algorithm with sub-pixel precision, capable of guiding on defocused stars. *Publications of the Astronomical Society of the Pacific*, 125(927):548, 2013.

[31] P. Seitzer et al. A search for optically faint GEO debris. Technical report, National Aeronautics and Space Administration Houston TX Lyndon B. Johnson, 2011.

[32] K. S. Jarviset al. Observations of the geosynchronous Earth orbital debris environment using NASA's CCD Debris Telescope. In *Space Debris*, volume 473, pages 95–99, 2001.

[33] T. Schildknecht et al. Optical observations of space debris in GEO and in highly-eccentric orbits. *Advances in Space Research*, 34(5):901–911, 2004.

[34] J. Africano et al. Understanding photometric phase angle corrections. In *4th European Conference on Space Debris*, volume 587, page 141, 2005.

[35] P. Papushev, Y. Karavaev, and M. Mishina. Investigations of the evolution of optical characteristics and dynamics of proper rotation of uncontrolled geostationary artificial satellites. *Advances in Space Research*, 43(9):1416–1422, 2009.

[36] C. R. Binz, M. A. Davis, B. E. Kelm, and C. I. Moore. Optical survey of the tumble rates of retired GEO satellites. Technical report, Naval Research Lab Washington DC, 2014.

[37] R. L. Cognion. Rotation Rates of Inactive Satellites Near Geosynchronous Earth Orbit. In *Proceedings of the Advanced Maui Optical and Space Surveillance Technologies Conference*, 2014.

[38] J. C. Hinks and J. L. Crassidis. Angular velocity bounds via light curve glint duration. In *AIAA Guidance, Navigation, and Control Conference*, page 0627, 2016.

[39] A. A. Albuja et al. The YORP effect on the GOES 8 and GOES 10 satellites: A case study. *Advances in Space Research*, 61(1):122–144, 2018.

[40] T. Cardona et al. BVRI photometric observations and light-curve analysis of GEO objects. *Advances in Space Research*, 58(4):514–527, 2016.

[41] H. D. Curtis. *Orbital mechanics for engineering students*. Butterworth-Heinemann, 2013.

[42] A. Milani et al. Orbit determination with very short arcs. I admissible regions. *Celestial Mechanics and Dynamical Astronomy*, 90(1-2):57–85, 2004.